# Magnetospheric Multiscale observations of the Source Region of Energetic Electron Microinjections along the Dusk-side, High-latitude Magnetopause Boundary Layer

K. Nykyri <sup>1</sup>, J. Johnson <sup>2</sup>, E. Kronberg <sup>3</sup>, D. Turner <sup>4</sup>, S. Wing <sup>4</sup>, I. Cohen <sup>4</sup>, K. Sorathia <sup>4</sup>, X. Ma <sup>1</sup>, B. Burkholder <sup>1</sup>, G. Reeves <sup>5</sup>, J. Fennell <sup>6</sup>

<sup>1</sup>Department of Physical Sciences and Centre for Space and Atmospheric Research, Embry-Riddle Aeronautical University,

Daytona Beach, FL, USA

<sup>2</sup>Andrews University, Berrien Springs, MI, USA

<sup>3</sup>University of Munich, Germany

<sup>4</sup>Applied Physics Laboratory, Maryland, MD, USA

<sup>5</sup>Los Alamos National Laboratory, NM, USA

<sup>6</sup>Aerospace Corporation, CA, USA

# **Key Points:**

13

- MMS detected dispersionless electron microinjections in ULF magnetic field wave depressions at the high-latitude magnetosphere.
- ULF waves were consistent with mirror mode waves created by the drift mirror instability.

Corresponding author: K. Nykyri, nykyrik@erau.edu

#### Abstract

19

23

27

31

44

47

The present paper demonstrates the first observations by the Magnetospheric Multiscale (MMS) mission of the counter-streaming energetic electrons and trapped energetic protons, localized in the magnetic field depressions between the mirror mode peaks, in the Earth's dusk sector high-latitude magnetosphere. This region is characterized by high plasma beta, strong ion temperature anisotropy and intermediate plasma density between magnetospheric and magnetosheath plasma. We show that these plasma conditions are unstable for the drift mirror instability. The counter-streaming electron feature resembles those of the previously reported energetic electron microinjections, but without the energy-time dispersion signature. This suggests that MMS is passing through one of the potential microinjection source regions. The energetic ion data in the present study is mainly used to estimate the scale size of the mirror mode structures.

## Plain Language Summary

Understanding the physical mechanisms that result in energetic electron acceleration and loss within the Van Allen radiation belts has been an active area of research for decades, and due to advances made possible by the Van Allen probe mission are now relatively well understood. However, the origin of the several 10s to 100s of keV seed population that can be accelerated to relativistic energies has remained more elusive. It is well known that magnetic reconnection and related secondary processes in the Earth's magnetotail during substorms can accelerate particles and inject them inward toward the radiation belts. In this paper we show the first observations of a possible source region of 10s to 100s of keV electrons and protons at the dayside of the Earth's high-latitude magnetosphere. Four MMS spacecraft periodically encountered high fluxes of energetic electrons at wide energy range which were streaming both parallel and anti-parallel to the magnetic field. Enhanced fluxes of counter-streaming energetic electrons and trapped protons were observed between magnetic field peaks of the ULF waves identified as mirror mode peaks. The source region of these electrons and protons are likely the large diamagnetic cavities created by magnetic reconnection.

#### 1 Introduction

Understanding the origin and formation of the relativistic electrons trapped in the Earth's belts had been under debate for decades [Reeves et al., 2013]. The Van Allen Probe spacecraft was the first to distinguish between the two major candidate processes, i) local acceleration, and ii) remote acceleration of the source population outside of the radiation belts. It was found that the observed radial profiles of phase space densities were consistent with local acceleration "in the heart of the radiation belts" and are inconsistent with a predominantly radial acceleration process [Reeves et al., 2013; Boyd et al., 2018]. However, both of these mechanisms require a seed population. Both case studies [Jaynes et al., 2015] and analysis of the statistical properties [Boyd et al., 2016] of the radiation belt seed particles are supporting a scenario of a stepwise acceleration process, where tens to hundreds of keV seed population is first accelerated via inward radial transport into the heart of the outer belt (4  $\lesssim L \lesssim$  6) and then subsequently accelerated up to multi-MeV energies via local acceleration and further inward radial transport. One candidate mechanism to generate this seed population is the substorm activity [Turner et al., 2017] where magnetic reconnection in the magnetotail at substorm onset, and subsequent field dipolarization fronts result in rapid Earthward transport of 10s to 100s of keV electrons and ions, a process called "injections" [Gabrielse et al., 2014]. Depending when the particles at different energies arrive at the observing spacecraft, the energy-time "injection" signature can be dispersionless, dispersed or inversely dispersed (see Gabrielse et al. [2014] and references therein).

More localized in scale-size than the traditional injections, the energetic electron "microinjections", have been observed in the morning sector of the inner plasma sheet by Interball Spacecraft [Sarafopoulos, 2002] during the growth phase of a magnetospheric substorm. The Magnetosphere Multiscale (MMS) mission detected dispersive microinjections in the dusk to midnight region [Fennell et al., 2016]. The observed timing of the flux enhancements in different energy ranges was not the same but higher energies were observed first, followed by the lower energy particles. This energy dispersion signature of the 50-400 keV electrons is consistent with the source region being at earlier magnetic local times (MLT) [Fennell et al., 2016] alongside the duskside magnetopause. Gradientcurvature drift is energy-dependent with higher energies drifting faster which creates an energy-dispersed signature at locations outside the source region. MHD simulations with solar wind and IMF conditions taken during a dispersive microinjection event, combined with test particle tracing suggest that the microinjections in the dusk to pre-midnight sector, can be mapped to the magnetopause boundary with observed microburst periodicity timescales consistent with Kelvin-Helmholtz wave and flux transfer event activity [Kavosi et al., 2018]. However, the direct observations of the source of microinjections have remained elusive.

In the present paper we show MMS observations of the dispersionless microinjections of the 29-149 keV electrons in the pre-dusk sector of the high-latitude magnetosphere during several hours of relatively steady southward, duskward IMF. The microinjections coincide with the magnetic field depressions of the Pc5 range Ultra Low Frequency (ULF) range fluctuations, identified here as mirror-mode waves. Mirror-mode waves are typically observed in the magnetosheath [Soucek et al., 2008; Dimmock et al., 2015] downstream of the quasi-perpendicular shock driven by the ion temperature anisotropy  $(T_{\perp}/T_{\parallel} > 1)$  in a high beta plasma. Sub-ion scale magnetic holes, reminiscent of mirror mode dips, have been commonly observed in the Earth's magnetotail [Gershman et al., 2016; Zhang et al., 2017; Shustov et al., 2019]. Here, we show first observations of the locally generated mirror mode waves in this region of geospace and provide new insight into the formation of the energetic electron microinjections.

#### 2 Data

67

68

83

93

103

104

106

107

108

110

111

112

114

115

116

All magnetospheric data are the level 2 data from NASA's MMS satellites [Burch et al., 2016]. We use Fast Plasma Investigation (FPI) [Pollock et al., 2016] for the lower energy ion and electron energy spectra and moments; Flux Gate Magnetometers (FGM) [Russell et al., 2016; Torbert et al., 2016] for the magnetic field. Energetic electron and ion distribution and pitch angle (PA) data comes from the Fly's Eye Energetic Particle Spectrometer (FEEPS) [Blake et al., 2016] instrument. Energetic proton (electron) and PA data comes also from the Energetic Ion Spectrometer (EIS) [Mauk et al., 2016]. The electric field is from Spin-Plane and Axial Double Probes (EDP) [Lindqvist et al., 2016; Ergun et al., 2016; Torbert et al., 2016]. The versions of the data files used are v4.18.0.cdf, v3.3.0.cdf, v6.1.2.cdf, v6.0.1.cdf, v3.0.1.cdf, v2.1.0.cdf for FGM (survey mode), FPI (fast mode), FEEPS (survey mode), EIS (survey mode), and EDP (fast mode), respectively. Solar wind conditions are taken from the OMNI (http://omniweb.gsfc.nasa.gov/) database [King and Papitashvili, 2005].

### 3 MMS Observations

On 2nd of October 2015 the four MMS spacecraft moved from the high-latitude dayside boundary layer (from  $r_{GSM} \approx [8, 6, -4]R_E$ ) at 8:30 UT into the pre-dusk sector magnetosphere ( $r_{GSM} \approx [5.4, 9, -4.9]R_E$ ) at 16:00 UT where they encountered quasiperiodic ULF waves with counter-streaming energetic electrons between magnetic field peaks of the ULF depressions for  $\approx 3$  hrs at 15.8 to 16.6 MLT. Figure 1 shows the overview plot (using data from MMS1) between 8:30 and 19:10 UT of low energy electron energy

118

120

122

124

125

128

132

133

135

137

139

141

145

149

150

152

158

162

163

165

166

167

168

169

spectra (a), magnetic field strength (b), PA distribution (PAD) of 90-149 keV electrons (c), plasma density and temperature (d), as well as IMF observations from OMNI (e) propagated to bow-shock nose (see Figure caption for more details). While the IMF  $B_z$  shows three oscillations during  $\approx 10$  hrs, it mostly remains negative and has a strong and steady duskward component. The interval from 8:40-10:20 UT shows magnetic field depressions (b) with high fluxes of trapped energetic electrons (c). It has been shown that these diamagnetic cavities (DMCs) were formed by low-latitude reconnection [Nykyri et al., 2019] about 10  $R_E$  from the MMS location. The IMF  $B_z$  and dynamic pressure (not shown) variations result in the motion of the magnetopause relative to MMS, such that MMS moves from DMC-region into low temperature, high density magnetosheath (≈10:30 UT), then to magnetospheric boundary layer (BL) at  $\approx 11:30$ , followed by transition back to magnetosheath (≈ 11:50). After 13:30 UT MMS mostly remains at the BL characterized by high temperature and lower density. At 16:20-19:10 UT significant fluxes (comparable to fluxes of trapped electrons at 8:30-10:10) of the 90-149 keV electrons (from EIS) show counter-streaming feature (c) and are associated with magnetic field depressions. Panels f, g and h show MMS trajectory in GSM coordinates projected on different -planes at 9:00 - 19:00 UT, depicted by the T96 magnetic field model [Tsyganenko, 1996]. Because spacecraft separations are small (≤ 30 km), all MMS spacecraft detect the same large plasma and field structures. Based on the T96 model, MMS is about 2  $R_E$  from the magnetopause in the high-latitude southern magnetosphere at 17:28 UT (see caption for more details).

Figure 2 presents high and low energy plasma and field observations during 16:00 -19:10 UT (see caption for more details on panels). During this interval the fluxes of the energetic ions (a) gradually decrease from 16:00 to 19:10 UT, while the low energy ion component (b) shows periodic flux enhancements. Energetic electrons (c) show periodic oscillations, matching the ion temperature enhancements (e) and magnetic field depressions (k). Plasma number density is typically below 1/cc (e), and plasma velocity (f) and magnetic field (h) show strong fluctuations. The low energy plasma and magnetic field pressure are anti-correlated (g) and roughly satisfy a local pressure balance while the total pressure gradually increases from 1 nPa at the beginning of the interval to 1.5 nPa observed at the end. The energetic (70-600 keV) ions (i) are mostly trapped, while the energetic electrons (j), observed in magnetic field depressions are mostly in the local loss cone and are counter-streaming. We refer to these periodic, enhanced fluxes of counter-streaming electrons as microinjections. Examining them at different energy ranges can reveal whether they are locally or remotely generated.

Figure 3 shows the EIS combined product of the energetic electron (b-d) and proton (e-j) PADs at different energy channels (see caption). Magnetic field strength (a) from MMS1 is shown for reference indicating that the enhanced counter-streaming electron and trapped proton fluxes are localized within magnetic field peaks (highlighted with vertical lines). The FEEPS combined electron product (k-n) from four MMS spacecraft shows electron PADs at different combined energy channels. Note that the FEEPS and EIS energy channels are at slightly different energy ranges. The 29-53 keV (b) and 40-70 keV (k) electrons have higher fluxes and typically (except for the first two enhancements at ≈16:14-16:26 UT) have more isotropic PADs than the higher energy electrons (c-d) and (l-n), which show more counter-streaming nature. Unlike the energy dispersed microinjections observed by Fennell et al. [2016], here the electron flux enhancements at different energy channels occur simultaneously (dispersionless), which suggest that spacecraft must be close to the source region of the electron microinjections. The bi-directional nature of these energetic electron PADs suggest that these are different than the "Energetic Electron Layer", which was first discovered at the high latitudes and reported to have more isotropic PADs by Meng and Anderson [1970].

The 147-232 keV protons (j), show two ion flux enhancements with more isotropic PADs at  $\approx$ 16:06 (1st vertical line) and  $\approx$ 16:16 UT (2nd vertical line). These flux enhance-

171

177

181

185

186

188

192

194

197

201

202

205

206

208

210

211

214

218

219

221

222

223

ments are observed few minutes later for 101-139 keV ions (i), while the 20-95 keV proton fluxes (e-h) show enhancements closer to 90 degrees, and are periodically modulated by the ULF waves throughout the interval. After 17:20 the 68 keV-232 keV protons (hj) become increasingly more 90 degrees in PAD and appear to be localized in magnetic field depressions of the ULF waves at 17:00-18:25 UT. Please note that the 70-600 keV FEEPS ion PADs (shown in Figure 2) correspond well to the EIS 68-95 keV energy PAD (the lowest energies  $\approx 70$  keV have the highest intensities in the 70-600 keV combined product). After 17:20 UT the proton fluxes become increasingly weaker at higher energies (i and j). These observations support the interpretation of a localized source of protons with wide energy range (20 keV to 232 keV) at  $\approx$  16-16:25 UT and a constant source of 20-95 keV protons that exist throughout the interval at 16:00-17:10 UT. The ULF wave modulation of the proton fluxes at energies of 20-139 keV and absence at higher energies is indicative of a "leaky wave trap" which could be explained by a gyro-radius effect: if the ULF wave has smaller scale size than the ion gyro-radius, the protons do not remain trapped within the wave but are effectively gradient and curvature drifting away from the source region. During this interval the magnetic field varies from 12 nT to 49 nT so the gyro-radius of the protons close to 90 degree PA varies from 460 km to 1870 km, from 830 km to 1700 km, and from 1020 km to 2080 km for the 24 keV, 80 keV and 119 keV protons (midpoint energies of the energy channels shown in panels e, h and j), respectively. The proton fluxes at these energies drop at higher magnetic field value suggesting that the minimum perpendicular wave length,  $\lambda_{\perp}$  of the ULF waves is of the order of 1000 km, thus much larger than the  $\approx$  30 km separation of the MMS spacecraft.

The local linear theory instability condition for the Drift Mirror (DM) instability can be derived assuming the low frequency ( $\omega \ll \omega_i$ ) and long wave length limits, and a bi-Maxwellian distribution for the ions (cold electrons) as follows [Hasegawa, 1969; Soto-Chavez et al., 2019]

$$\beta_{\perp}(p_{\perp}/p_{\parallel}-1) > 1,\tag{1}$$

where  $\omega_i$  is ion angular frequency,  $p_\perp$  ( $p_\parallel$ ) is the perpendicular (parallel) plasma pressure, and  $\beta_\perp = p_\perp/p_B$  is the perpendicular plasma beta. Figure 4 shows plasma parameters (a-g) together with drift mirror instability (DMI) criteria from Equation 1 (h) (see caption). The plasma and magnetic pressure are periodically anti-correlated which is a typical signature of the mirror mode waves. Here the mirror wave period is about 5 min. However, here the density is low and nearly constant (see Figure 2e), so the variations in the plasma pressure are dominated by the variations in ion temperature. The yellow columns highlight the intervals where DM instability criteria is well above unity. This occurs in the magnetic field depressions in the region of high plasma beta and enhanced perpendicular ion temperature. The mirror-modes exhibit themselves in two distinct modes: peaks and dips. The peaks, such as observed here, are typically observed in an unstable plasma, while mirror structures within the stable region appear almost exclusively as dips [Joy et al., 2006; Soucek et al., 2008].

The electron (i) and ion (j) temperature anisotropy vs parallel plasma beta scatter plots (color coded by electron and ion specific entropies) reveal that electron plasma is stable to electron firehose (EF) instability [Gary and Nishimura, 2003] but few data points satisfy and several are close to whistler (W) instability criteria [Gary et al., 2012] (i). However, the fitting parameters vary with the assumed maximum growth rate, which depends on the electron velocity distribution functions that for the present event appear to be more complex than the typically assumed bi-Maxwellians. Here the electrons can be partly closely perpendicular at 10-30 keV energies as well as partly counter-streaming at the energy ranges of 29-89 keV (Figure 3b and c, and Figure 4a), and mostly counter-streaming at low energies ( $\leq$  10 keV) (b). See supplementary information for the analysis of electron (Figure S1) and ion (Figure S2) PADs at 10 eV to 30 keV energy range. The threshold criteria for mirror mode, proton cyclotron, fluid fire hose, parallel firehose and oblique fire hose instabilities are plotted after equations and fitting parameters from Hellinger et al. [2006] (j). The ion plasma, measured by FPI, has the highest fluxes at 10

keV to 30 keV energy range with mostly transverse PADs (see Figure S2), consistent also with protons measured by EIS at 20-41 keV range (Figure 3e and 3f).

The plots show that the mirror mode growth rate is relatively large. It is likely the case that the plasma anisotropy suddenly increased and there was not time to establish a steady state. Rapid compression (faster than the mirror mode growth time) could be responsible for development of anisotropy beyond the DMI criteria. Development of the instability is not necessarily quasilinear. Gyrokinetic simulations (ion velocity distribution is averaged over the ion gyro-angle), have shown development of mirror mode peaks which can lead to particle trapping [Porazik and Johnson, 2013], where the peaks narrowed and grew in conjunction with Fermi acceleration of resonant (slow moving) particles. Note that here the instability threshold is not satisfied everywhere (only near the troughs) which means that just plotting all data may lead to a mixture of apparently stable and unstable regions within a growing mirror mode structure. The trough regions where electrons are trapped likely remain above the threshold, but may saturate due to ion trapping.

#### 4 Discussion and Conclusions

224

225

227

233

234

237

275

276

278

280

282

286

287

289

291

293

295

297

303

307

308

310

311

312

The present observations suggest a new source for the energetic electron microinjections. We show that the ion temperature anisotropy in the high-latitude magnetosphere, characterized by high plasma beta, creates fruitful conditions for the drift mirror instability. The mirror mode waves are observed in their peak mode. They have a  $\approx 5$  minute periodicity and thus correspond to Pc5 band of the ULF frequency range. Here the mirror mode waves and microinjections are observed within the boundary layer as the plasma density remains relatively steady and does not reach magnetosheath values with the mirror mode periodicity. The mirror mode waves modulate the electron and proton fluxes with the same periodicity such that the highest counter-streaming electron fluxes and trapped protons are observed between magnetic field peaks. The counter-streaming electron signature could be related to the Fermi-acceleration [Wu et al., 2006; Porazik and Johnson, 2013]. The smallest electron fluxes are observed during the strong, high frequency electric field fluctuations (see Figure S3) which could be a consequence of wave-induced scattering [Kunz et al., 2014] and merits further investigation.

As the mirror mode waves are typically observed in the magnetosheath, downstream of the quasi-perpendicular shock driven by the ion temperature anisotropy  $(T_{\perp}/T_{\parallel} > 1)$ , an urgent question is to understand what generates the strong ion temperature asymmetry and high plasma beta at the high-latitude magnetosphere? The mirror modes and microinjections are observed after earlier diamagnetic cavity encounters [Nykyri et al., 2019] that show presence of trapped energetic electrons (and ions) with the same fluxes and energy ranges. The characteristic feature of the particle acceleration in the diamagnetic cavities is that particles gain tens of keV in energy perpendicular to magnetic field in few minutes, thus resulting in temperature anisotropy [Nykyri et al., 2012; Burkholder et al., 2021]. The diamagnetic cavity scale sizes can be on the order of few  $R_E$  [Nykyri et al., 2011; Burkholder et al., 2021], thus they can act as a large volume reservoir for the energetic particles. During this event the diamagnetic cavities were observed only  $\approx 4~R_E$  away from the microinjection site (see red ovals in Figure 1), therefore it is possible MMS is relatively close to the cavity boundary. Considering the relatively steady southward and duskward IMF for several hours, the low latitude reconnection, which created the cavities at southern hemisphere [Nykyri et al., 2019], could have operated relatively steadily providing continuous source for cavity (and temperature anisotropy) generation in this location. Alternatively, these high-energy electrons could also potentially leak from the diamagnetic cavity formed during the prevailing IMF orientation ( $B_z < 0$  and  $B_y > 0$ ) at the sunward-dusk sector of the northern cusp [Nykyri et al., 2011; Nykyri et al., 2019] due to possible reconnection as predicted by T96 model (see yellow star in Figure 11f), be reflected at southern hemisphere and captured at field depressions between mirror mode peaks.

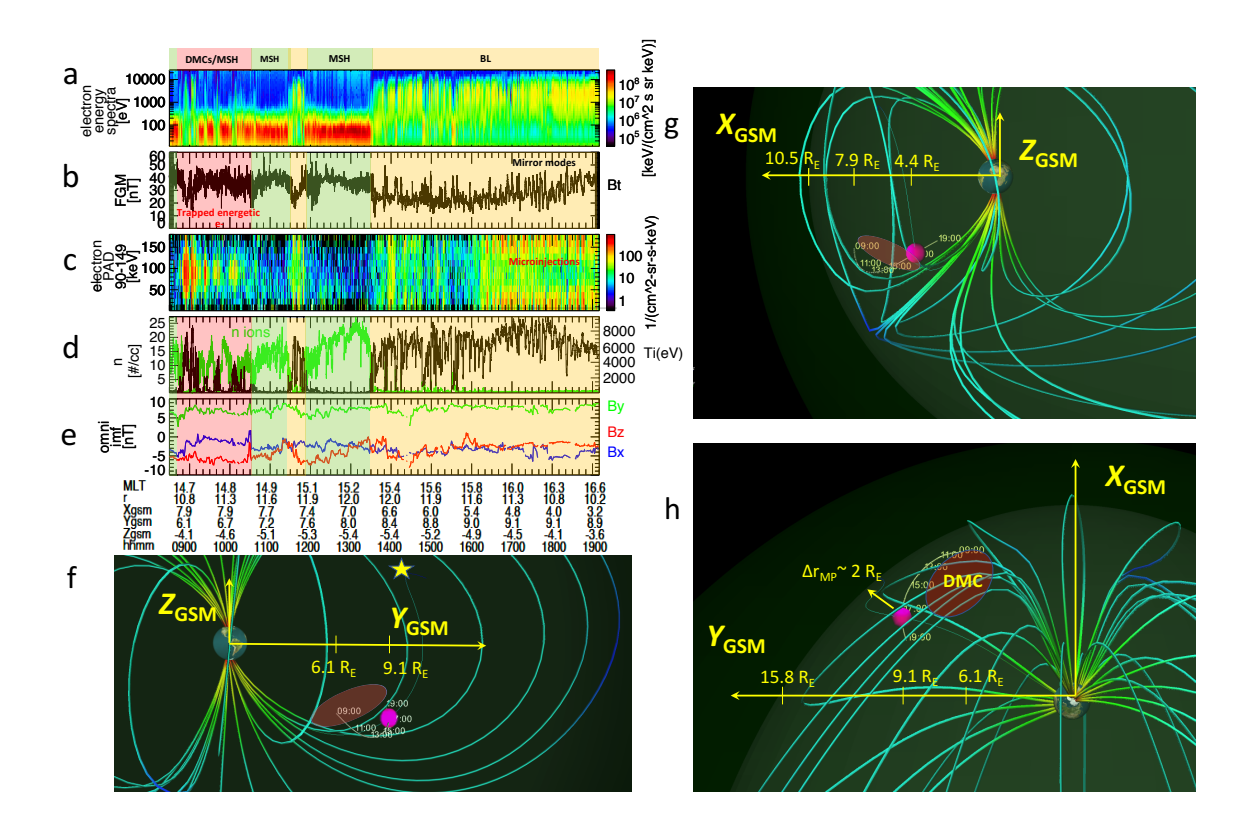


**Figure 1.** Overview plot of the MMS 1 data on 2nd of October, 2015 at 8:30 - 19:10 UT. The panels from top to bottom present omni-directional electron spectrogram of low energy electrons (a), magnetic field strength (b), PAD of the 90-149 keV energy electrons from EIS (c), plasma density (green) and temperature (black) (d), and the IMF components (e). The colored boxes depict the diamagnetic cavity (DMC) encounters formed by low latitude reconnection (DMC=red), magnetosheath (msh=green), and high-latitude boundary layer (BL=yellow). MMS location at 17:28 UT and trajectory on 2nd of October, 2015 at 9:00 - 19:00 UT in the Earth's magnetosphere which is plotted using Tsyganenko 1996 (T96) [*Tsyganenko*, 1996] magnetic field model in y,  $z_{GSM}$  (f), x,  $z_{GSM}$  (g), and y,  $z_{GSM}$  (h)-planes. The location and approximate geometry of the diamagnetic cavity, as determined from simulations and MMS observations in study by *Nykyri et al.* [2019], is shown with red oval. T96 model magnetosphere is run at 17:28 UT with  $\mathbf{B} = [-5.5, 7.0, -2.0]$ nT, solar wind dynamic pressure, Pdyn of 1.6 nPa, and Dst of -22 nT, determined from OMNI. The Pdyn varied between 16:00-19:00 UT from 1.71 to 1.35 nPa which made MMS distance to the model magnetopause vary from 2.23  $R_E$  to 1.77  $R_E$ , while it remained within the magnetosphere. The magnetic field line from MMS is traced and clipped at the magnetopause, which shows approximate location (yellow star) of the magnetic reconnection at 17:28 UT based on the T96 model.

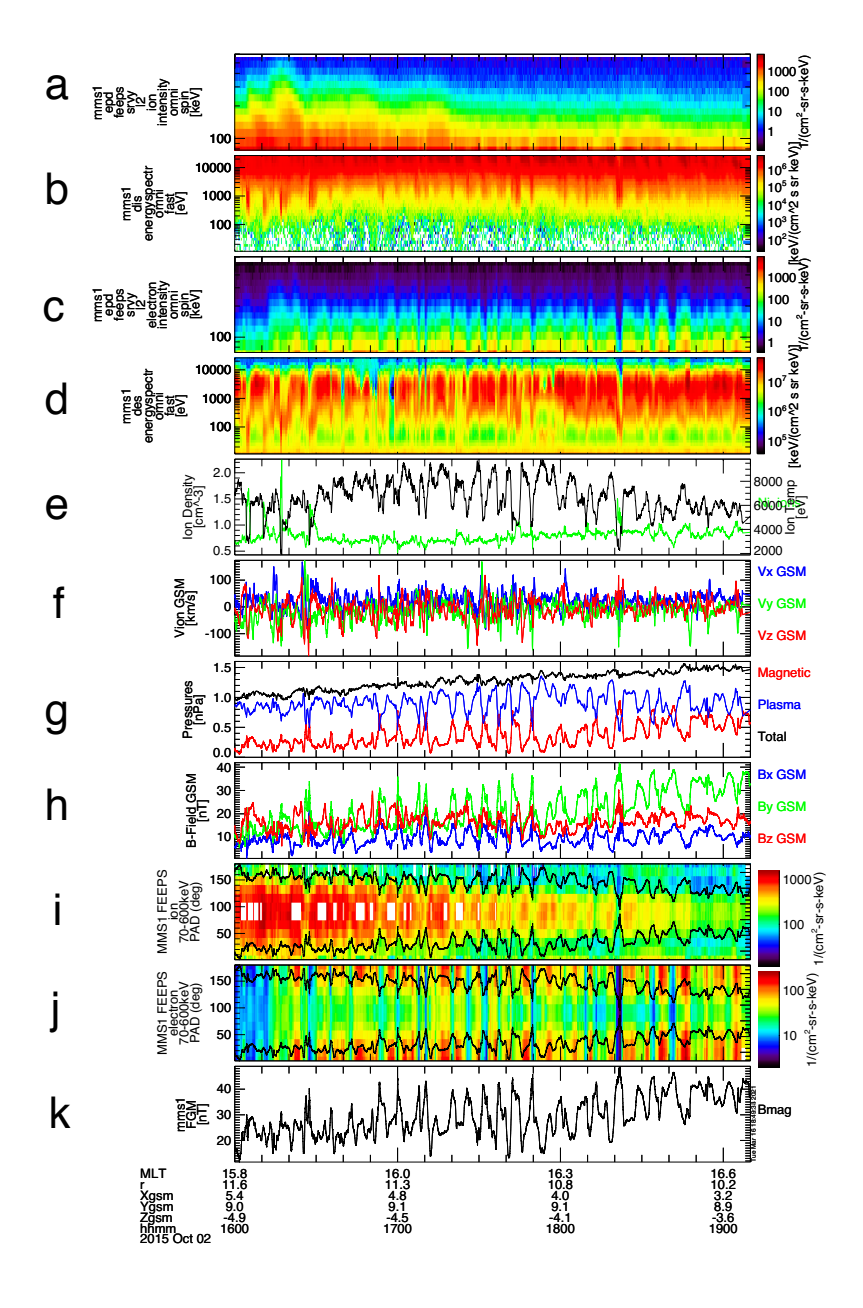
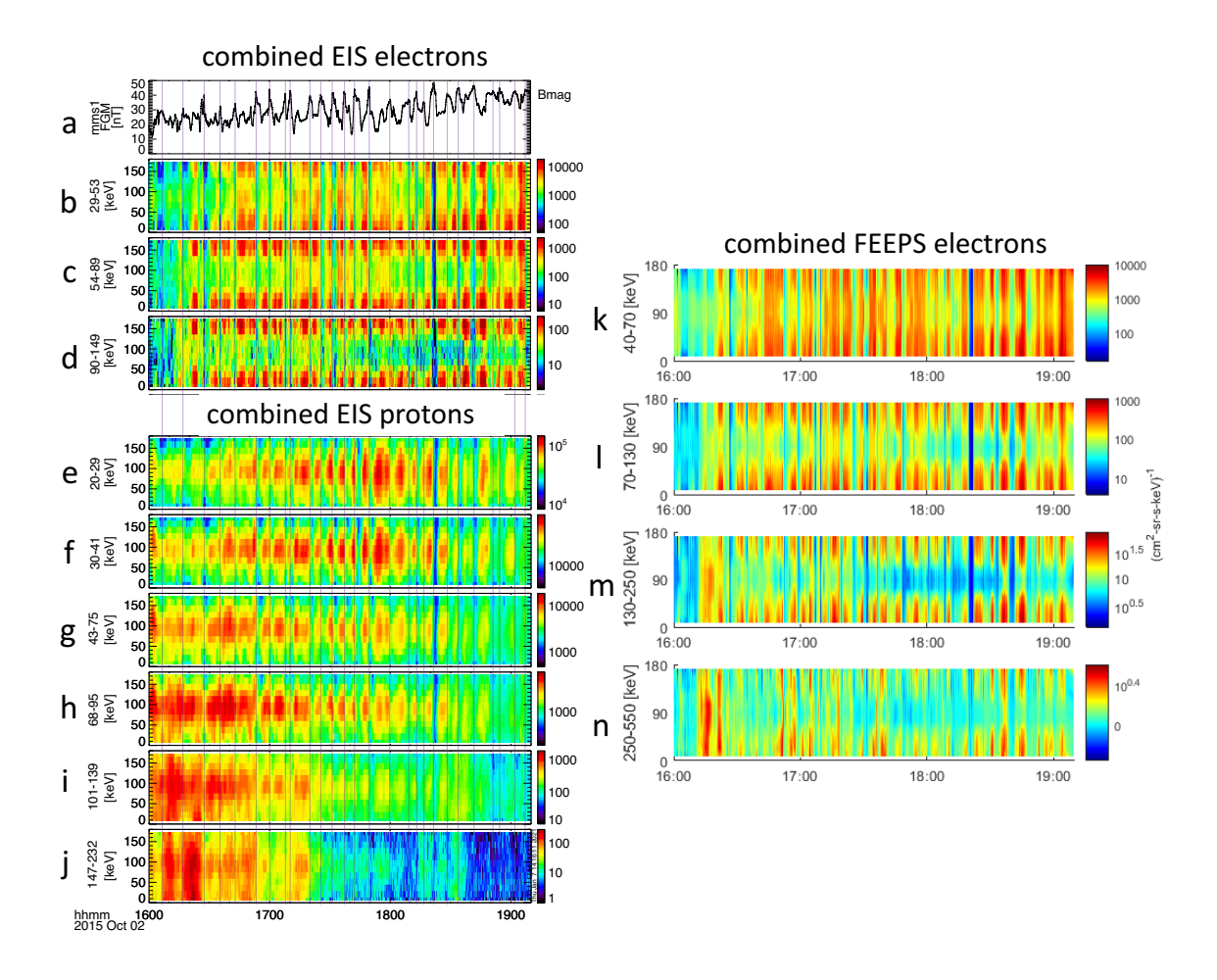
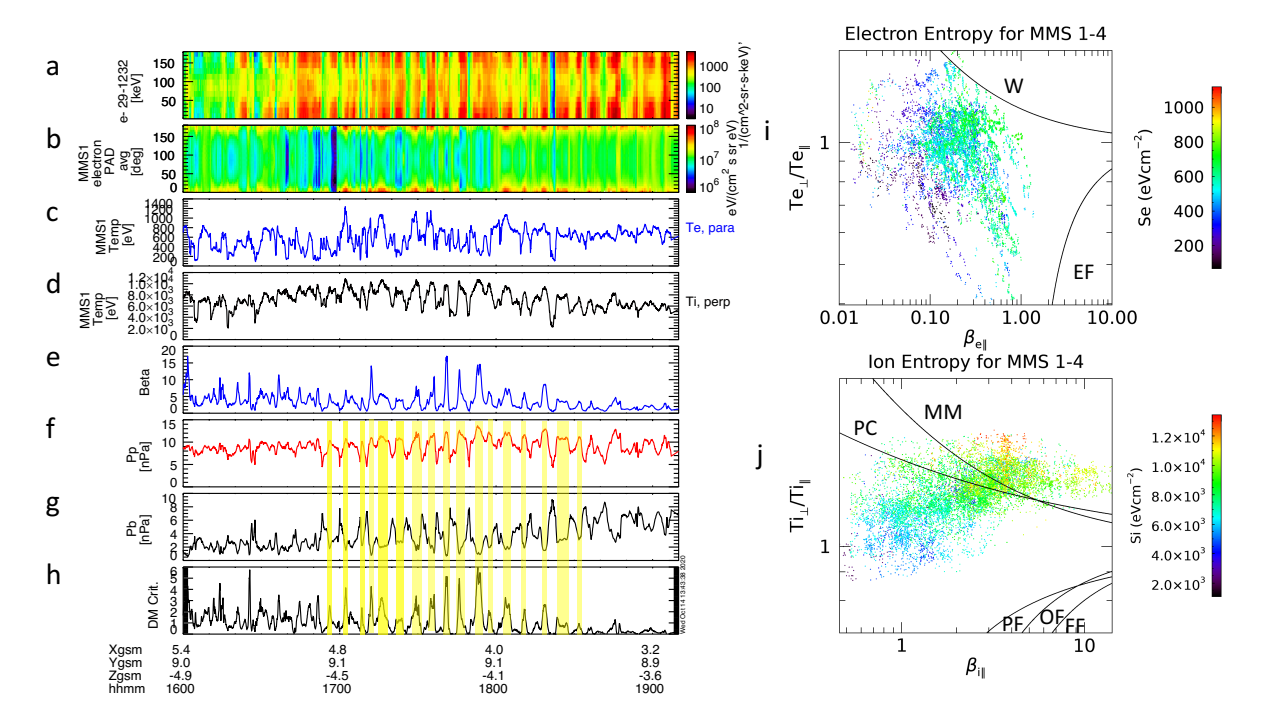


Figure 2. Overview plot of the MMS 1 data on 2nd of October, 2015 at 16:00 - 19:10 UT. The panels from top to bottom present the omni-directional 70-600 keV (a) and 100 eV-30 keV (b) ion spectrograms; same for electrons are shown in panels c and d; plasma density (green) and temperature (black) (e); ion velocity (f), pressures (g), magnetic field (h), PADs of 70-600 keV ions (i) and electrons (j), and the magnetic field strength (k). The local trapping angle,  $\alpha = \arctan(\frac{1}{\sqrt{B_M/B-1}})$ , is shown as black envelopes in panels (i and j) and is computed in same way as in [Nykyri et al., 2012; Breuillard et al., 2018; Ahmadi et al., 2018; Nykyri et al., 2019], where a constant magnetic field value,  $B_M = 49 \, \mathrm{nT}$  at the mirror point is used (which is also the maximum magnetic field observed by MMS during this interval) and B is the local magnetic field magnitude observed at each given point between 16:00-19:10 UT.



**Figure 3.** Observations of PADs of the fluxes of the energetic electrons from the EPD instrument at different energy channels: 29-53 keV (b), 54-89 keV (c), and 90-149 keV (d). These are the combined electron fluxes using the MMS1 and MMS3 EIS data. The PADs of the fluxes of the combined energetic ions from all four spacecraft at 20-29 keV (e), 30-41 keV (f), 43-75 keV (g), 68-95 keV (h), 101-139 keV (i), and 147-232 keV (j) energies are shown for comparison from EIS. The phxtof (extof) data product is used for the three lowest (highest) energy channels. The four spacecraft combined FEEPS electrons are shown for the energy ranges of 40-70 keV (k), 70-130 keV (l), 130-250 keV (m), and 250-550 keV (n).



**Figure 4.** Plasma parameters at 16:00-19:10 UT. The plasma parameters show PADs of 29-1232 keV electrons from EIS (a); PADs of FPI low energy energy electrons (b); electron parallel temperature (c) and ion perpendicular temperature (d) from FPI; plasma beta (e), plasma pressure (f), magnetic pressure (g), and drift mirror mode criteria (h). The electron (i) and ion (j) temperature anisotropy vs parallel plasma beta scatter plots together with electron whistler (EW), electron firehose (EF), mirror mode (MM), ion cyclotron (IC), and ion fire hose (IF) instability contours.

While this is the first observation of the mirror mode waves and microinjections observed in this region of geospace, we expect this frequently occur in this location for similar solar wind and IMF conditions. The temperature anisotropy is likely to form anywhere in the high-latitude magnetosphere where the diamagnetic cavities can form and stay stable sufficiently long for the particle acceleration to occur. Since the cavity formation happens somewhere in the vicinity of the northern or southern cusps for any IMF orientation [Nykyri et al., 2011; Burkholder et al., 2021], this mechanism could be a potential source for microinjections and help partly explain the radiation belt electron seed population. MHD simulations with test particles have revealed how a new outer radiation belt can be created during a handful of discrete, injections by the gradient trapping and transport [Sorathia et al., 2018].

Furthermore, this high-latitude boundary layer can also be unstable to the KHI [Nykyri et al., 2020; Hwang et al., 2012] which can also generate temperature anisotropy [Ma et al., 2019]. Global 3-D simulations addressing both the KHI and mirror-mode generation remain to be developed to fully understand the coupling of these processes.

#### Acknowledgments

313

314

316

320

321

323

325

326

327

338

328 The work by KN, XM, and JJ were funded by NASA grant #NNX17AI50G, and work by BB and KN were supported by NASA grant #80NSSC8K1381. KS was supported 330 by NASA grant # 80NSSC8K1381 via a subcontract to JHU/APL. EK is supported by 331 German Research Foundation (DFG) under number KR 4375/2-1 within SPP "Dynamic Earth". MMS data were downloaded through the MMS Science Data Center at https://lasp.colorado.edu/mms/sdc/public/. We recognize the efforts from MMS instrument teams and also acknowledge the use of SPEDAS software used for the analysis [Angelopoulos et al., 2019]. We acknowledge use 335 of NASA/GSFC's Space Physics Data Facility's OMNIWeb (http://omniweb.gsfc.nasa.gov) service and Orbit Visualization Tool (https://ovt.irfu.se). 337

## References

D. Malaspina, K. Paulson, K. Germaschewski, S. Eriksson, K. Goodrich, R. Torbert, 340 O. Le Contel, R. J. Strangeway, C. T. Russell, J. Burch, and B. Giles (2018), Generation 341 of electron whistler waves at the mirror mode magnetic holes: Mms observations and 342 pic simulation, Journal of Geophysical Research: Space Physics, 123(8), 6383-6393, doi:10.1029/2018JA025452. 344 Angelopoulos, V., P. Cruce, A. Drozdov, E. Grimes, N. Hatzigeorgiu, D. King, D. Lar-345 son, J. Lewis, J. McTiernan, D. Roberts, C. Russell, T. Hori, Y. Kasahara, A. Kumamoto, A. Matsuoka, Y. Miyashita, Y. Miyoshi, I. Shinohara, M. Teramoto, J. Faden, 347 A. Halford, M. McCarthy, R. Millan, J. Sample, D. Smith, L. Woodger, A. Masson, A. Narock, K. Asamura, T. Chang, C.-Y. Chiang, Y. Kazama, K. Keika, S. Matsuda, T. Segawa, K. Seki, M. Shoji, S. Tam, N. Umemura, B.-J. Wang, S.-Y. Wang, R. Redmon, J. Rodriguez, H. Singer, J. Vandegriff, S. Abe, M. Nose, A. Shinbori, Y.-M. 351 Tanaka, S. UeNo, L. Andersson, P. Dunn, C. Fowler, J. Halekas, T. Hara, Y. Harada, C. Lee, R. Lillis, D. Mitchell, M. Argall, K. Bromund, J. Burch, I. Cohen, M. Galloy, B. Giles, A. Jaynes, O. Le Contel, M. Oka, T. Phan, B. Walsh, J. Westlake, F. Wilder, S. Bale, R. Livi, M. Pulupa, P. Whittlesey, A. DeWolfe, B. Harter, E. Lucas, U. Auster, 355 J. Bonnell, C. Cully, E. Donovan, R. Ergun, H. Frey, B. Jackel, A. Keiling, H. Korth, 356 J. McFadden, Y. Nishimura, F. Plaschke, P. Robert, D. Turner, J. Weygand, R. Candey, R. Johnson, T. Kovalick, M. Liu, R. McGuire, A. Breneman, K. Kersten, and 358 P. Schroeder (2019), The space physics environment data analysis system (spedas), Space Science Reviews, 215(1), doi:10.1007/s11214-018-0576-4. 360 Blake, J. B., B. H. Mauk, D. N. Baker, P. Carranza, J. H. Clemmons, J. Craft, W. R. Crain, A. Crew, Y. Dotan, J. F. Fennell, R. H. Friedel, L. M. Friesen, F. Fuentes, 362 R. Galvan, C. Ibscher, A. Jaynes, N. Katz, M. Lalic, A. Y. Lin, D. M. Mabry, 363

Ahmadi, N., F. D. Wilder, R. E. Ergun, M. Argall, M. E. Usanova, H. Breuillard,

- T. Nguyen, C. Pancratz, M. Redding, G. D. Reeves, S. Smith, H. E. Spence, and J. Westlake (2016), The Fly's Eye Energetic Particle Spectrometer (FEEPS) Sensors for the Magnetospheric Multiscale (MMS) Mission, *Space Science Reviews*, 199, 309–329, doi:10.1007/s11214-015-0163-x.
  - Boyd, A. J., H. E. Spence, C.-L. Huang, G. D. Reeves, D. N. Baker, D. L. Turner, S. G. Claudepierre, J. F. Fennell, J. B. Blake, and Y. Y. Shprits (2016), Statistical properties of the radiation belt seed population, *Journal of Geophysical Research: Space Physics*, 121(8), 7636–7646, doi:10.1002/2016JA022652.
  - Boyd, A. J., D. L. Turner, G. D. Reeves, H. E. Spence, D. N. Baker, and J. B. Blake (2018), What causes radiation belt enhancements: A survey of the van allen probes era, *Geophysical Research Letters*, 45(11), 5253–5259, doi: https://doi.org/10.1029/2018GL077699.

370

371

373

375

376

377

378

380

384

385

387

390

397

398

400

403

405

407

- Breuillard, H., O. Le Contel, T. Chust, M. Berthomier, A. Retino, D. L. Turner, R. Nakamura, W. Baumjohann, G. Cozzani, F. Catapano, A. Alexandrova, L. Mirioni, D. B. Graham, M. R. Argall, D. Fischer, F. D. Wilder, D. J. Gershman, A. Varsani, P.-A. Lindqvist, Y. V. Khotyaintsev, G. Marklund, R. E. Ergun, K. A. Goodrich, N. Ahmadi, J. L. Burch, R. B. Torbert, G. Needell, M. Chutter, D. Rau, I. Dors, C. T. Russell, W. Magnes, R. J. Strangeway, K. R. Bromund, H. Wei, F. Plaschke, B. J. Anderson, G. Le, T. E. Moore, B. L. Giles, W. R. Paterson, C. J. Pollock, J. C. Dorelli, L. A. Avanov, Y. Saito, B. Lavraud, S. A. Fuselier, B. H. Mauk, I. J. Cohen, and J. F. Fennell (2018), The properties of lion roars and electron dynamics in mirror mode waves observed by the magnetospheric multiscale mission, *Journal of Geophysical Research: Space Physics*, 123(1), 93–103, doi:10.1002/2017JA024551.
  - Burch, J. L., T. E. Moore, R. B. Torbert, and B. L. Giles (2016), Magnetospheric Multiscale Overview and Science Objectives, *Space Science Reviews*, *199*, 5–21, doi: 10.1007/s11214-015-0164-9.
  - Burkholder, B. L., K. Nykyri, and X. Ma (2021), Magnetospheric multiscale statistics of high energy electrons trapped in diamagnetic cavities, *Journal of Geophysical Research: Space Physics*, *126*(1), e2020JA028,341, doi:https://doi.org/10.1029/2020JA028341, e2020JA028341 2020JA028341.
  - Dimmock, A. P., A. Osmane, T. I. Pulkkinen, and K. Nykyri (2015), A statistical study of the dawn-dusk asymmetry of ion temperature anisotropy and mirror mode occurrence in the terrestrial dayside magnetosheath using THEMIS data, *Journal of Geophysical Research: Space Physics*, 120(7), 5489–5503, doi:10.1002/2015JA021192.
  - Ergun, R. E., S. Tucker, J. Westfall, K. A. Goodrich, D. M. Malaspina, D. Summers,
    J. Wallace, M. Karlsson, J. Mack, N. Brennan, B. Pyke, P. Withnell, R. Torbert,
    J. Macri, D. Rau, I. Dors, J. Needell, P.-A. Lindqvist, G. Olsson, and C. M. Cully
    (2016), The Axial Double Probe and Fields Signal Processing for the MMS Mission,
    Space Science Reviews, 199, 167–188, doi:10.1007/s11214-014-0115-x.
- Fennell, J. F., D. L. Turner, C. L. Lemon, J. B. Blake, J. H. Clemmons, B. H. Mauk, A. N. Jaynes, I. J. Cohen, J. H. Westlake, D. N. Baker, J. V. Craft, H. E. Spence, G. D. Reeves, R. B. Torbert, J. L. Burch, B. L. Giles, W. R. Paterson, and R. J. Strangeway (2016), Microinjections observed by mms feeps in the dusk to midnight region, *Geophysical Research Letters*, 43(12), 6078–6086, doi:10.1002/2016GL069207.
- Gabrielse, C., V. Angelopoulos, A. Runov, and D. L. Turner (2014), Statistical characteristics of particle injections throughout the equatorial magnetotail, *Journal of Geophysical Research: Space Physics*, *119*(4), 2512–2535, doi:10.1002/2013JA019638.
  - Gary, S. P., and K. Nishimura (2003), Resonant electron firehose instability: Particle-incell simulations, *Physics of Plasmas*, 10(9), 3571–3576, doi:10.1063/1.1590982.
  - Gary, S. P., K. Liu, R. E. Denton, and S. Wu (2012), Whistler anisotropy instability with a cold electron component: Linear theory, *Journal of Geophysical Research: Space Physics*, 117(A7), doi:10.1029/2012JA017631.
- Gershman, D. J., J. C. Dorelli, A. F. Viñas, L. A. Avanov, U. Gliese, A. C. Barrie, V. Coffey, M. Chandler, C. Dickson, E. A. MacDonald, C. Salo, M. Holland, Y. Saito, J.-A.

Sauvaud, B. Lavraud, W. R. Paterson, R. Torbert, L.-J. Chen, K. Goodrich, C. T. Russell, R. J. Strangeway, B. L. Giles, C. J. Pollock, T. E. Moore, and J. L. Burch (2016), Electron dynamics in a subproton-gyroscale magnetic hole, *Geophysical Research Letters*, 43(9), 4112–4118, doi:https://doi.org/10.1002/2016GL068545.

422

424

425

427

428

430

431

432

433

435

437

438

440

441

443

444

446

447

449

450

452

453

454

455

456

- Hasegawa, A. (1969), Drift mirror instability in the magnetosphere, *The Physics of Fluids*, *12*(12), 2642–2650, doi:10.1063/1.1692407.
- Hellinger, P., P. Trávníček, J. C. Kasper, and A. J. Lazarus (2006), Solar wind proton temperature anisotropy: Linear theory and wind/swe observations, *Geophysical Research Letters*, *33*(9), doi:10.1029/2006GL025925.
- Hwang, K.-J., M. L. Goldstein, M. M. Kuznetsova, Y. Wang, A. F. Vikas, and D. G. Sibeck (2012), The first in situ observation of kelvin-helmholtz waves at high-latitude magnetopause during strongly dawnward interplanetary magnetic field conditions, *Journal of Geophysical Research: Space Physics*, 117(A8), 2156–2202, doi: 10.1029/2011JA017256, a08233.
- Jaynes, A. N., D. N. Baker, H. J. Singer, J. V. Rodriguez, T. M. Loto'aniu, A. F. Ali, S. R. Elkington, X. Li, S. G. Kanekal, S. G. Claudepierre, J. F. Fennell, W. Li, R. M. Thorne, C. A. Kletzing, H. E. Spence, and G. D. Reeves (2015), Source and seed populations for relativistic electrons: Their roles in radiation belt changes, *Journal of Geophysical Research: Space Physics*, 120(9), 7240–7254, doi:10.1002/2015JA021234.
- Joy, S. P., M. G. Kivelson, R. J. Walker, K. K. Khurana, C. T. Russell, and W. R. Paterson (2006), Mirror mode structures in the jovian magnetosheath, *Journal of Geophysical Research: Space Physics*, 111(A12), doi:https://doi.org/10.1029/2006JA011985.
- Kavosi, S., H. E. Spence, J. F. Fennell, D. L. Turner, H. K. Connor, and J. Raeder (2018), Mms/feeps observations of electron microinjections due to kelvin-helmholtz waves and flux transfer events: A case study, *Journal of Geophysical Research: Space Physics*, 123(7), 5364–5378, doi:10.1029/2018JA025244.
  - King, J. H., and N. E. Papitashvili (2005), Solar wind spatial scales in and comparisons of hourly Wind and ACE plasma and magnetic field data, *Journal of Geophysical Research* (*Space Physics*), 110, A02104, doi:10.1029/2004JA010649.
- Kunz, M. W., A. A. Schekochihin, and J. M. Stone (2014), Firehose and mirror instabilities in a collisionless shearing plasma, *Phys. Rev. Lett.*, *112*, 205,003, doi: 10.1103/PhysRevLett.112.205003.
- Lindqvist, P.-A., G. Olsson, R. B. Torbert, B. King, M. Granoff, D. Rau, G. Needell, S. Turco, I. Dors, P. Beckman, J. Macri, C. Frost, J. Salwen, A. Eriksson, L. Åhlén, Y. V. Khotyaintsev, J. Porter, K. Lappalainen, R. E. Ergun, W. Wermeer, and S. Tucker (2016), The Spin-Plane Double Probe Electric Field Instrument for MMS, *Space Science Reviews*, 199, 137–165, doi:10.1007/s11214-014-0116-9.
- Ma, X., P. A. Delamere, K. Nykyri, B. Burkholder, B. Neupane, and R. C. Rice (2019), Comparison between fluid simulation with test particles and hybrid simulation for the kelvin-helmholtz instability, *Journal of Geophysical Research: Space Physics*, 124(8), 6654–6668, doi:10.1029/2019JA026890.
- Mauk, B. H., J. B. Blake, D. N. Baker, J. H. Clemmons, G. D. Reeves, H. E. Spence,
  S. E. Jaskulek, C. E. Schlemm, L. E. Brown, S. A. Cooper, J. V. Craft, J. F. Fennell,
  R. S. Gurnee, C. M. Hammock, J. R. Hayes, P. A. Hill, G. C. Ho, J. C. Hutcheson,
  A. D. Jacques, S. Kerem, D. G. Mitchell, K. S. Nelson, N. P. Paschalidis, E. Rossano,
  M. R. Stokes, and J. H. Westlake (2016), The Energetic Particle Detector (EPD) Investigation and the Energetic Ion Spectrometer (EIS) for the Magnetospheric Multiscale
  (MMS) Mission, Space Science Reviews, 199, 471–514, doi:10.1007/s11214-014-0055-5.
- Meng, C. I., and K. A. Anderson (1970), A layer of energetic electrons (>40 kev) near
   the magnetopause, *Journal of Geophysical Research* (1896-1977), 75(10), 1827–1836,
   doi:https://doi.org/10.1029/JA075i010p01827.
- Nykyri, K., A. Otto, E. Adamson, E. Dougal, and J. Mumme (2011), Cluster observations of a cusp diamagnetic cavity: Structure, size, and dynamics, *Journal of Geophysical Research (Space Physics)*, *116*, A03228, doi:10.1029/2010JA015897.

Nykyri, K., A. Otto, E. Adamson, E. Kronberg, and P. Daly (2012), On the origin of high-energy particles in the cusp diamagnetic cavity, *Journal of Atmospheric and Solar- Terrestrial Physics*, 87, 70–81, doi:10.1016/j.jastp.2011.08.012.

475

478

479

481

483

484

485

486

488

492

493

495

496

497

499

500

502

503

505

506

507

508

509

510

512

515

516

522

523

524

- Nykyri, K., C. Chu, X. Ma, S. A. Fuselier, and R. Rice (2019), First MMS observation of energetic particles trapped in high-latitude magnetic field depressions, *Journal of Geophysical Research: Space Physics*, *124*(1), 197–210, doi:10.1029/2018JA026131.
- Nykyri, K., X. Ma, B. Burkholder, R. Rice, J. Johnson, E.-K. Kim, P. Delamere, A. Michael, K. Sorathia, D. Lin, S. Merkin, S. Fuselier, J. Broll, O. Le Contel, D. Gershman, I. Cohen, B. Giles, R. J. Strangeway, C. T. Russell, and J. Burch (2020), MMS Observations of the Multi-Scale Wave Structures and Parallel Electron Heating in the Vicinity of the Southern Exterior Cusp, *Journal of Geophysical Research: Space Physics*, n/a, e2019JA027,698, doi:https://doi.org/10.1029/2019JA027698.
- Pollock, C., T. Moore, A. Jacques, J. Burch, U. Gliese, Y. Saito, T. Omoto, L. Avanov, A. Barrie, V. Coffey, J. Dorelli, D. Gershman, B. Giles, T. Rosnack, C. Salo, S. Yokota, M. Adrian, C. Aoustin, C. Auletti, S. Aung, V. Bigio, N. Cao, M. Chandler, D. Chornay, K. Christian, G. Clark, G. Collinson, T. Corris, A. De Los Santos, R. Devlin, T. Diaz, T. Dickerson, C. Dickson, A. Diekmann, F. Diggs, C. Duncan, A. Figueroa-Vinas, C. Firman, M. Freeman, N. Galassi, K. Garcia, G. Goodhart, D. Guererro, J. Hageman, J. Hanley, E. Hemminger, M. Holland, M. Hutchins, T. James, W. Jones, S. Kreisler, J. Kujawski, V. Lavu, J. Lobell, E. LeCompte, A. Lukemire, E. Mac-Donald, A. Mariano, T. Mukai, K. Narayanan, Q. Nguyan, M. Onizuka, W. Paterson, S. Persyn, B. Piepgrass, F. Cheney, A. Rager, T. Raghuram, A. Ramil, L. Reichenthal, H. Rodriguez, J. Rouzaud, A. Rucker, Y. Saito, M. Samara, J.-A. Sauvaud, D. Schuster, M. Shappirio, K. Shelton, D. Sher, D. Smith, K. Smith, S. Smith, D. Steinfeld, R. Szymkiewicz, K. Tanimoto, J. Taylor, C. Tucker, K. Tull, A. Uhl, J. Vloet, P. Walpole, S. Weidner, D. White, G. Winkert, P.-S. Yeh, and M. Zeuch (2016), Fast Plasma Investigation for Magnetospheric Multiscale, Space Science Reviews, 199, 331-406, doi:10.1007/s11214-016-0245-4.
  - Porazik, P., and J. R. Johnson (2013), Gyrokinetic particle simulation of nonlinear evolution of mirror instability, *Journal of Geophysical Research: Space Physics*, *118*(11), 7211–7218, doi:https://doi.org/10.1002/2013JA019308.
  - Reeves, G. D., H. E. Spence, M. G. Henderson, S. K. Morley, R. H. W. Friedel, H. O. Funsten, D. N. Baker, S. G. Kanekal, J. B. Blake, J. F. Fennell, S. G. Claudepierre, R. M. Thorne, D. L. Turner, C. A. Kletzing, W. S. Kurth, B. A. Larsen, and J. T. Niehof (2013), Electron acceleration in the heart of the van allen radiation belts, *Science*, 341(6149), 991–994, doi:10.1126/science.1237743.
- Russell, C. T., B. J. Anderson, W. Baumjohann, K. R. Bromund, D. Dearborn, D. Fischer, G. Le, H. K. Leinweber, D. Leneman, W. Magnes, J. D. Means, M. B. Moldwin, R. Nakamura, D. Pierce, F. Plaschke, K. M. Rowe, J. A. Slavin, R. J. Strangeway, R. Torbert, C. Hagen, I. Jernej, A. Valavanoglou, and I. Richter (2016), The Magnetospheric Multiscale Magnetometers, *Space Science Reviews*, 199, 189–256, doi: 10.1007/s11214-014-0057-3.
  - Sarafopoulos, D. V. (2002), Dispersive and repetitive pc5 mode microinjections in the inner magnetosphere, *Geophysical Research Letters*, 29(8), 26–1–26–4, doi: 10.1029/2001GL014067.
- Shustov, P. I., X.-J. Zhang, P. L. Pritchett, A. V. Artemyev, V. Angelopoulos, E. V. Yushkov, and A. A. Petrukovich (2019), Statistical properties of sub-ion magnetic holes in the dipolarized magnetotail: Formation, structure, and dynamics, *Journal of Geophysical Research: Space Physics*, *124*(1), 342–359, doi: https://doi.org/10.1029/2018JA025852.
  - Sorathia, K. A., A. Y. Ukhorskiy, V. G. Merkin, J. F. Fennell, and S. G. Claudepierre (2018), Modeling the depletion and recovery of the outer radiation belt during a geomagnetic storm: Combined mhd and test particle simulations, *Journal of Geophysical Research: Space Physics*, 123(7), 5590–5609, doi:https://doi.org/10.1029/2018JA025506.

Soto-Chavez, A. R., L. J. Lanzerotti, J. W. Manweiler, A. Gerrard, R. Cohen, Z. Xia, L. Chen, and H. Kim (2019), Observational evidence of the drift-mirror plasma instability in earth's inner magnetosphere, *Physics of Plasmas*, 26(4), 042,110, doi: 10.1063/1.5083629.

530

532

533

535

537

539

542

545

547

549

- Soucek, J., E. Lucek, and I. Dandouras (2008), Properties of magnetosheath mirror modes observed by Cluster and their response to changes in plasma parameters, *Journal of Geophysical Research (Space Physics)*, 113, 4203.
- Torbert, R. B., C. T. Russell, W. Magnes, R. E. Ergun, P.-A. Lindqvist, O. LeContel,
  H. Vaith, J. Macri, S. Myers, D. Rau, J. Needell, B. King, M. Granoff, M. Chutter,
  I. Dors, G. Olsson, Y. V. Khotyaintsev, A. Eriksson, C. A. Kletzing, S. Bounds, B. Anderson, W. Baumjohann, M. Steller, K. Bromund, G. Le, R. Nakamura, R. J. Strangeway, H. K. Leinweber, S. Tucker, J. Westfall, D. Fischer, F. Plaschke, J. Porter, and
  K. Lappalainen (2016), The FIELDS Instrument Suite on MMS: Scientific Objectives, Measurements, and Data Products, Space Science Reviews, 199, 105–135, doi: 10.1007/s11214-014-0109-8.
  - Tsyganenko, N. A. (1996), Effects of the solar wind conditions on the global magnetospheric configuration as deduced from data-based field models, in *Proceedings of the ICS-3 Conference on substorms (Versailles, France May 12-17, 1996)*, pp. 181–185, ESA SP-389.
- Turner, D. L., J. F. Fennell, J. B. Blake, S. G. Claudepierre, J. H. Clemmons, A. N. Jaynes, T. Leonard, D. N. Baker, I. J. Cohen, M. Gkioulidou, A. Y. Ukhorskiy, B. H. Mauk, C. Gabrielse, V. Angelopoulos, R. J. Strangeway, C. A. Kletzing, O. Le Contel, H. E. Spence, R. B. Torbert, J. L. Burch, and G. D. Reeves (2017), Multipoint observations of energetic particle injections and substorm activity during a conjunction between magnetospheric multiscale (mms) and van allen probes, *Journal of Geophysical Research: Space Physics*, 122(11), 11,481–11,504, doi:10.1002/2017JA024554.
- Wu, P., T. A. Fritz, B. Larvaud, and E. Lucek (2006), Substorm associated magnetotail energetic electrons pitch angle evolutions and flow reversals: Cluster observation, *Geophysical Research Letters*, *33*(17), doi:https://doi.org/10.1029/2006GL026595.
- Zhang, X.-J., A. Artemyev, V. Angelopoulos, and R. B. Horne (2017), Kinetics of sub-ion scale magnetic holes in the near-earth plasma sheet, *Journal of Geophysical Research:* Space Physics, 122(10), 10,304–10,317, doi:https://doi.org/10.1002/2017JA024197.